Super-resolution ultrasonic imaging of close reflectors in coarse-grained steels based on a deconvolution approach

Nans Laroche, Ewen Carcreff, Sébastien Bourguignon, Jérôme Idier, Aroune Duclos, Pierre-Emile Lhuillier

▶ **To cite this version:**

Nans Laroche, Ewen Carcreff, Sébastien Bourguignon, Jérôme Idier, Aroune Duclos, et al.. Super-resolution ultrasonic imaging of close reflectors in coarse-grained steels based on a deconvolution approach. Journal of Nondestructive Evaluation, 2022, 41 (66), 10.1007/s10921-022-00900-2 . hal-03240520

HAL Id: hal-03240520
https://hal.science/hal-03240520

Submitted on 28 May 2021

HAL is a multi-disciplinary open access archive for the deposit and dissemination of scientific research documents, whether they are published or not. The documents may come from teaching and research institutions in France or abroad, or from public or private research centers.

L'archive ouverte pluridisciplinaire **HAL**, est destinée au dépôt et à la diffusion de documents scientifiques de niveau recherche, publiés ou non, émanant des établissements d'enseignement et de recherche français ou étrangers, des laboratoires publics ou privés.

Super-resolution ultrasonic imaging of close reflectors in coarse-grained steels based on a deconvolution approach

Nans Laroche[a,b], Ewen Carcreff[a], Sébastien Bourguignon[b], Jérôme Idier[b], Aroune Duclos[c] and Pierre-Emile Lhuillier[d]

[a]The Phased Array Company/DB-SAS, 13 rue du Bois Briand, Impasse de la Turquoise, 44300 Nantes, France
[b]LS2N, 1 rue de la Noë, 44321 Nantes, France
[c]LAUM, avenue Olivier Messiaen, 72085 Le Mans, France
[d]EDF R&D, Site des renardières, avenue des renardières, 77250 Ecuelles, France

ARTICLE INFO

Keywords:
Ultrasonic imaging, deconvolution, inverse problem, coarse-grained steel, super-resolution.

ABSTRACT

Ultrasonic inspection of coarse-grained steels is a common challenge in various industrial fields. This task is often difficult because of acoustic scattering that creates structural noise in the ultrasonic signals and images. This drives inspections using low-frequency probes at the cost of a lower resolution of standard delay and sum (DAS) imaging techniques, such as the well-known total focusing method (TFM). The purpose of this paper is to present and evaluate the performances of an image reconstruction technique that aims at improving the resolution when inspecting industrial coarse-grained materials. An image deconvolution problem (with spatially varying blur) is formulated, relying on a forward model that links the TFM image to the acoustic reflectivity map. A particular attention is paid to the estimation of the PSF used for the deconvolution approach in an experimental context. The experiments are based on an austenitic-ferritic sample insonified using array probes at 3 MHz and 5 MHz placed in contact. The goal is to resolve two close reflectors corresponding to side drilled holes (SDH) with diameter 0.4 mm spaced by 0.4 mm edge to edge and positioned at different depths (10, 20, 30, 40 mm). This configuration corresponds to a critical case where the distance between the two reflectors is significantly inferior to the Rayleigh distance, that is the resolution limit of a DAS imaging system. These are typical cases where the employed frequency is actually too low and where a higher frequency probe should be used, which is not possible in practice, because it would affect the detection capability due to higher noise level. As predicted by the Rayleigh criterion, TFM is not able to separate the reflectors. The proposed image reconstruction method successfully resolves the majority of the reflectors with a rather accurate distance estimation. In the context of coarse-grained structure inspection, this approach enables the use of low-frequency probes, in order to improve the signal-to-noise ratio, while keeping high resolution capability.

1. Introduction

Ultrasonic imaging is a common procedure for nondestructive testing (NDT) of essential elements in many fields such as aeronautics, power generation or oil and gas industry. In the power generation domain, stainless steel materials are commonly employed because of their good resistance to high temperatures and mechanical stress. Such materials often have a coarse-grained structure. During ultrasonic testing (UT), their highly heterogeneous structure creates scattering of the ultrasonic waves, which generates structural noise in the ultrasonic signals and images. Scattering then creates acoustic attenuation, impacting the high frequency content of the propagated ultrasonic waves [1]. For this reason, relatively low frequency probes (around $2-3$ MHz) are used in this type of situation [2, 3], which limits the resolution of the imaging system.

In the present paper, the goals are twofold. First, our aim is to increase the contrast and denoise the image in order to improve the flaw detection capability. A second objective consists in improving the resolution, that is, the capability to separate close reflectors. Delay and sum (DAS) techniques are standard software beamformers that perform synthetic focusing in every point of the region of interest [4]. The total focusing method (TFM) [5, 6] is a DAS technique applied to full matrix capture (FMC) data—the full set of inter-element responses of the probe. TFM achieves good image quality because of its high number of recorded signals. Nevertheless, like all DAS techniques, it suffers from poor resolution and contrast in many cases. This is particularly true when inspecting coarse-grained materials, because of the employed low-frequency probes and of the structural noise corrupting the images.

Several techniques based on the Decomposition of the Time Reversal Operator (DORT) have been proposed [7, 8, 9], which mainly aim to increase the signal-to-noise ratio (SNR). Regularized inversion methods are efficient to address both resolution and SNR issues [10]. Inversion of the raw radio-frequency (RF) data was proposed in [11, 12], which is efficient but relatively slow due to the large amount of data. Other recent inverse methods that directly process the beamformed (BF) images can be seen as image deconvolution methods [13, 14]. In this case, it was shown that the computation speed could be dramatically increased because BF datasets are much smaller than RF datasets, while the resulting loss in image quality was found to be quite moderate [14]. In this paper, we present an image deconvolution method based on [14] for the ultrasonic imaging of coarse-grained steel, and we study its ability to improve the resolu-

ORCID(s):

tion in the context of sub-wavelength reflectors detection in scattering material.

The paper is organized as follows. In Section 2, the acquisition process and the associated standard beamforming method are detailed. Then, the image deconvolution method proposed in [14] is described in Section 3. In Section 4, the method is evaluated and compared to TFM imaging for inspection of an austenitic-ferritic stainless steel sample containing close side drilled holes (SDH) with 0.4 mm diameter. Finally, conclusion and perspectives are given in Section 5.

2. Data acquisition and standard TFM beamforming

The acquisition scheme of TFM is called full matrix capture (FMC). It consists in recording the elementary signals from all transmitter-receiver pairs of the array. If N_{el} is the number of elements in the array, the data are denoted $y_{ij}(t)$, where $i = 1 \dots N_{\text{el}}$ is the transmitter index, $j = 1 \dots N_{\text{el}}$ is the receiver index, and t stands for time. The total number of A-scans for a single dataset is hence N_{el}^2. In FMC, ultrasonic waves are transmitted independently by each transducer and collected by all of them, which is considered as a heavy procedure. Nevertheless, it contains a wide variety of exploitable information (longitudinal and shear modes, mode conversions, surface waves, *etc.*) [15].

The standard way to beamform the FMC data is the TFM beamformer. The intensity of the TFM image at any point with coordinates (x, z) is computed as:

$$o_{\text{TFM}}(x,z) = \sum_{i=1}^{N_{\text{el}}} \sum_{j=1}^{N_{\text{el}}} y_{ij}\big(\tau_{i,j}(x,z)\big), \tag{1}$$

where $\tau_{i,j}(x,z)$ is the time of flight from transmitter i to the point (x,z) and back to receiver j. Similarly to other DAS beamformers, the TFM consists in synthetically focusing the ultrasonic signals at all points of the region of interest.

Let $\boldsymbol{y}$ denote a column vector gathering all A-scans and let $\boldsymbol{o}_{\text{TFM}}$ denote a column vector collecting the pixel values of the beamformed TFM image. Equation (1) is a linear operation that can be written as:

$$\boldsymbol{o}_{\text{TFM}} = \mathbf{B}\boldsymbol{y}, \tag{2}$$

where $\mathbf{B} \in \mathbb{R}^{N_x N_z \times N_{\text{el}}^2 N_t}$ is called the beamforming operator [12]. For each pixel in the region of interest, the corresponding row in $\mathbf{B}$ selects the nearest indices corresponding to the times of flight in all A-scans involved in the summation (1). In this work, a binary operator $\mathbf{B}$ is considered, but an interpolation law between closest indices could be used [4] as well as an apodization law considering directivity patterns [6].

Note that Equation (2) gives a general expression of DAS beamforming. It can describe many acquisition schemes such as plane waves [16] and diverging waves [17]. In the next sections of this paper, we consider an FMC/TFM framework, but it can basically be applied to any acquisition scheme.

3. Deconvolution of TFM images

3.1. Forward data model

The FMC data $\boldsymbol{y}$ presented in Section 2 can be modeled as a discrete linear model [12]:

$$\boldsymbol{y} = \mathbf{H}_t \boldsymbol{o} + \boldsymbol{n}_t, \tag{3}$$

where $\mathbf{H}_t \in \mathbb{R}^{N_{\text{el}}^2 N_t \times N_x N_z}$ is the waveform matrix containing ultrasonic elementary signatures at the times of flight corresponding to all combinations of A-scans and pixels. Vector $\boldsymbol{o}$ represents the unknown (vectorized) reflectivity map of the media and $\boldsymbol{n}_t$ stands for noise and model errors, and it is assumed to be zero-mean, white and Gaussian.

As shown in [14], model (3) can be projected in the space domain in order to define a forward model between the reflectivity map and the TFM image. Indeed, applying the beamforming operator $\mathbf{B}$ to Equation (3) gives:

$$\boldsymbol{o}_{\text{TFM}} = \mathbf{B}\mathbf{H}_t \boldsymbol{o} + \mathbf{B}\boldsymbol{n}_t = \mathbf{H}_s \boldsymbol{o} + \boldsymbol{n}_s, \tag{4}$$

with $\mathbf{H}_s = \mathbf{B}\mathbf{H}_t$ and $\boldsymbol{n}_s = \mathbf{B}\boldsymbol{n}_t$. Retrieving the reflectivity map $\boldsymbol{o}$ from the TFM image $\boldsymbol{o}_{\text{TFM}}$ is similar to an image deconvolution problem. Matrix $\mathbf{H}_s \in \mathbb{R}^{N_x N_z \times N_x N_z}$ represents a non-stationary 2D convolution operator, where the Point Spread Function (PSF) is different for each pixel because of the acquisition geometry. Each column of $\mathbf{H}_s$ corresponds to the PSF associated with a point-like reflector in the reflectivity map. Vector $\boldsymbol{n}_s$ corresponds to the Gaussian white noise component $\boldsymbol{n}_t$ on which the TFM beamforming has been applied. The resulting noise statistics is still Gaussian but not white, in particular the covariance of $\boldsymbol{n}_s$ also depends on the acquisition geometry [14]. A whitening strategy can be classically employed in order to deal with colored noise. It consists in applying a "pre-whitening" operator to model (4), such that the resulting noise term can be considered as white [18]. The resulting model then reads:

$$\boldsymbol{o}^{\text{w}}_{\text{TFM}} = \mathbf{H}^{\text{w}}_s \boldsymbol{o} + \boldsymbol{n}^{\text{w}}_s, \tag{5}$$

where $\boldsymbol{o}^{\text{w}}_{\text{TFM}}$ is the whitened TFM image and $\mathbf{H}^{\text{w}}_s$ is the (approximate) whitened forward operator. In [14], an interpolation model is proposed which achieves fast and accurate computation of this model.

3.2. Waveform model

The forward model (5) requires the knowledge of the two-dimensional PSF at each point, which depends on the inspection geometry (*via* the matrix $\mathbf{B}$ in Equation (2)) and on the time-domain ultrasonic waveform h that propagates in the medium (upon which matrix $\mathbf{H}_t$ is built in Equation (3)).

In the following, we consider an identical waveform for all transducers modeled as an asymmetric Gaussian wavelet [19]:

$$h(t, \boldsymbol{\Theta}) = e(t, \alpha, r, m)\cos(2\pi f_o t + \phi), \tag{6}$$

where $\boldsymbol{\Theta} = [\alpha, r, m, f_0, \phi]$ collects the wavelet parameters: f_0 is the center frequency, ϕ is the phase shift, and the asymmetric envelope function $e(t, \alpha, r, m)$ is defined as:

$$e(t, \alpha, r, m) = e^{-\alpha(1 - r\tanh(mt))t^2}. \tag{7}$$

The envelope function has two different decay rates: $\alpha(1+r)$ for negative t and $\alpha(1-r)$ for positive t. The parameter m tunes the transition rate between the two parts. Such asymmetric model may accurately represent an ultrasonic waveform envelope, which generally decays more slowly than it raises.

In practice, the parameters $\boldsymbol{\Theta}$ must be estimated through a calibration procedure prior to inspection. In the case of coarse-grained materials, this is a difficult challenge due to structural noise, so that A-scans are very noisy. Therefore, we propose to estimate the parameters of the ultrasonic waveform from the TFM image, that coherently sums the ultrasonic echoes, so that the SNR is increased. We consider the TFM image of a pointwise reflector located at coordinates $(x_{\mathrm{PSF}}, z_{\mathrm{PSF}})$ in the material. Then, the A-scan signals can be written as:

$$y_{ij}(t) = h\big(t - \tau_{i,j}(x_{\mathrm{PSF}}, z_{\mathrm{PSF}}), \boldsymbol{\Theta}\big), \tag{8}$$

where $h(t, \boldsymbol{\Theta})$ is defined in (6). Then, the parameters $\boldsymbol{\Theta}$ are adjusted by fitting the data o_{TFM} with the image predicted by combining the TFM model (1) and model (8):

$$\min_{\boldsymbol{\Theta}} \left\| o_{\mathrm{TFM}}(x,z) - \sum_{i,j} h\big(\tau_{i,j}(x,z) - \tau_{i,j}(x_{\mathrm{PSF}}, z_{\mathrm{PSF}}), \boldsymbol{\Theta}\big) \right\|^2 .$$

In this paper, we use the Levenberg-Marquardt algorithm to solve this non-linear least squares optimization problem.

3.3. Inversion procedure

Ultrasonic transducers have a limited frequency range and consequently, the TFM image lacks information, in particular at high frequencies that contain the image details. Retrieving the reflectivity map from the whitened TFM image is an ill-posed problem [10]. Here, a classical regularization framework is employed, which consists in adding a penalization function to the least-squares misfit criterion to minimize:

$$\boldsymbol{o}_s = \arg\min_{\boldsymbol{o}} J_{\mathrm{LS}}(\boldsymbol{o}) + \phi(\boldsymbol{o}). \tag{9}$$

The term $J_{\mathrm{LS}}(\boldsymbol{o})$ is the standard least-squares criterion which is appropriate since the data have been whitened :

$$J_{\mathrm{LS}}(\boldsymbol{o}) := \left\| \boldsymbol{o}^{\mathrm{w}}_{\mathrm{TFM}} - \mathbf{H}^{\mathrm{w}}_s \boldsymbol{o} \right\|^2 . \tag{10}$$

The term $\phi(\boldsymbol{o})$ corresponds to the penalization function. We adopt a sparse regularization strategy to enhance high-frequency information in the solution. Spatial smoothness is also favored in order to reconstruct ultrasonic reflectors with some spatial extent. As a result, we get a hybrid penalization function:

$$\phi(\boldsymbol{o}) = \mu_1 \|\boldsymbol{o}\|_1 + \mu_2 \|\mathbf{D}\boldsymbol{o}\|^2 , \quad \mu_1, \mu_2 > 0, \tag{11}$$

where $\mathbf{D}\boldsymbol{o}$ is the image gradient and μ_1 and μ_2 are regularization parameters that balance between the data fitting term $J_{\mathrm{LS}}(\boldsymbol{o})$ and the regularization term $\phi(\boldsymbol{o})$. The tuning of these parameters is addressed in [12, 14]. The minimization of criterion (9) is performed using the Fast Iterative Shrinkage Thresholding Algorithm (FISTA) [20].

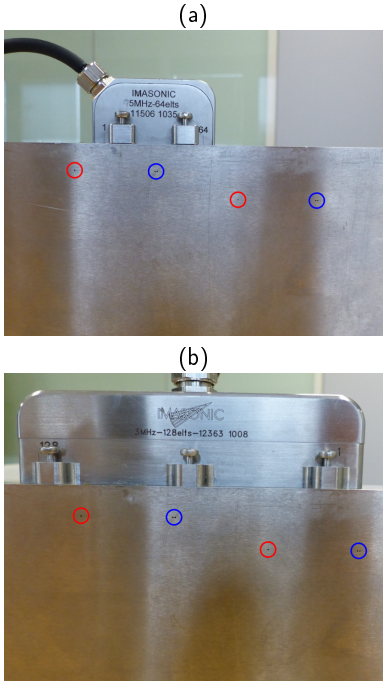

Figure 1: Picture of the sample used for experiments with 5 MHz probe (a) and with 3 MHz probe (b). The single SDH (respectively, the pairs of SDH) at 10 mm and 20 mm depths are circled in red (respectively, in blue).

4. Experimental results

4.1. Description of the experiments

The sample used for this study is represented in Figure 1. It is composed of austenitic-ferritic stainless steel with a coarse-grained structure. The sample contains SDH with 0.4 mm diameter, either isolated or paired, located at depths of 10, 20, 30 and 40 mm. The positions of the flaws are shown in the scheme of Figure 2. The distance between two close SDHs is equal to 0.4 mm edge-to-edge, that is, 0.8 mm center-to-center. The velocity of longitudinal waves has been measured at 5 700 m/s.

The RF data are acquired with the Pioneer system which is an open platform with fast acquisition speed (TPAC, West-Chester, USA). Each probe is placed in contact with the sample using coupling gel (see Figure 1). The sampling frequency is 50 MHz and the quantization corresponds to 14 bits. The acquisition procedure consists in FMC, detailed in Section 2. Two different probes are used in this study. The first has 64 elements and a central frequency of 5 MHz, and the second has 128 elements and a central frequency of 3 MHz (Imasonic, Voray-sur-l'Ognon, France). Their specifications are given in Table 1. Both probes have complementary properties. Indeed, a higher frequency probe (> 5 MHz) would be generally better suited to image such small defects in an homogeneous material. Nevertheless, higher frequencies are more strongly affected by scattering noise, so that a lower frequency probe would be preferred in order to achieve sufficient SNR enabling the detection of flaws, but then decreas-

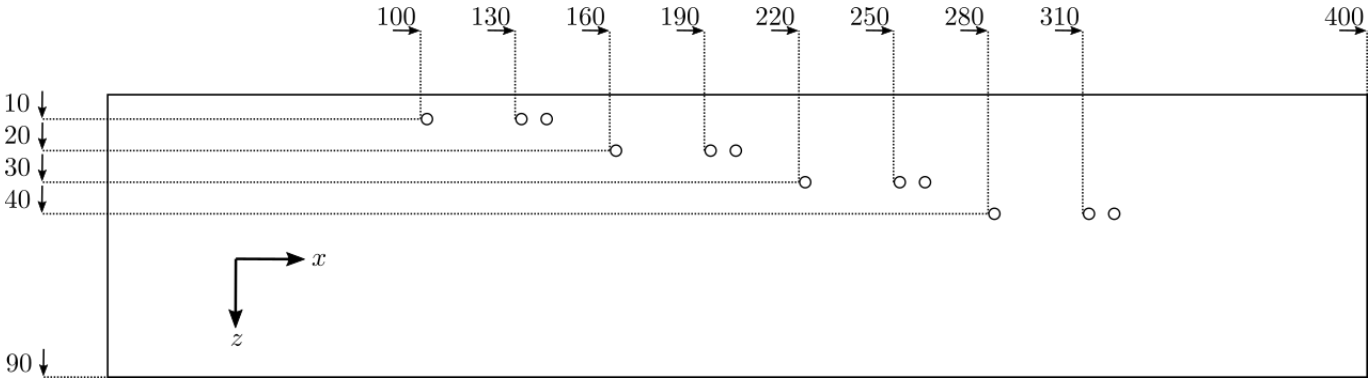

Figure 2: Scheme of the inspected piece, composed of series of single and double side drilled holes at different depths.

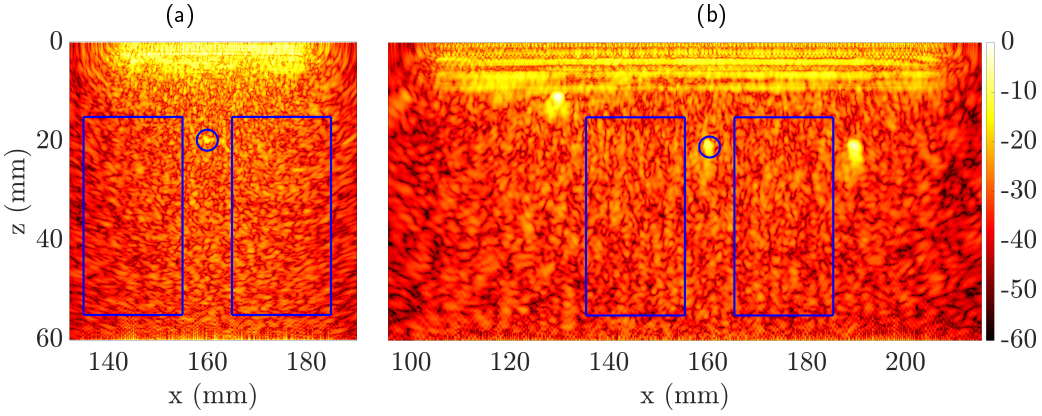

Figure 3: Zoom on the TFM images obtained with 5 MHz probe (a) and with 3 MHz probe (b) around $z = 20$ mm, and principle of SNR estimation. The reference scatterer is the single SDH circled in blue and the noise region is framed in blue.

ing the resolution of TFM imaging. Therefore, these experiments aim to study how the proposed inversion method, denoted by INV in the following, is able to achieve high resolution images with lower frequency probes.

In order to characterize the noise level for each problem (that is, for each probe and at the different inspection depths), we define the SNR from the TFM images as:

$$\mathrm{SNR} = 10 \log \frac{o_{\mathrm{TFM}}(x_{\mathrm{SDH}}, z_{\mathrm{SDH}})^2}{P_{\mathrm{noise}}}, \tag{12}$$

where $(x_{\mathrm{SDH}}, z_{\mathrm{SDH}})$ are the coordinates corresponding to the maximum amplitude of the single SDH and P_{noise} is the mean power in the noise region. Figure 3 illustrates the SNR definition at depth 20 mm, for the TFM images obtained with each probe. As discussed above, one can clearly see that the noise level is higher for 5 MHz data (SNR $\sim$ 20.9 dB) than for 3 MHz data (SNR $\sim$ 23.6 dB).

The difficulty of each problem is also measured in terms of resolution through the Rayleigh criterion $\mathcal{R}$ defined as:

$$\mathcal{R} = \frac{0.61\lambda}{\sin\theta}, \tag{13}$$

with λ denoting the wavelength and with $\tan\theta = D/(2z)$, where D is the full aperture of the array and z is the reflector depth. $\mathcal{R}$ corresponds to the resolving limit of a standard DAS beamformer [21]. In all following examples, the edge-to-edge distance between the two reflectors is close or inferior to the Rayleigh criterion. We focus on the capability of the TFM and INV to detect and separate the flaws, with depths varying from 10 to 40 mm.

# probe	1	2
Number of elements	64	128
Center frequency (MHz)	5	3
Pitch (mm)	0.6	0.8
Elevation (mm)	10	14
Wavelength (mm)	1.14	1.90

Table 1
Properties of the two probes used for inspection.

4.2. TFM image acquisition

As shown in Figure 1, the apertures of the two probes are too small to acquire the full data set from a single acquisition. Thus, the probes are successively located above each set of SDHs (see Figure 2). For each position, the corresponding TFM image is acquired. The imaged zone along

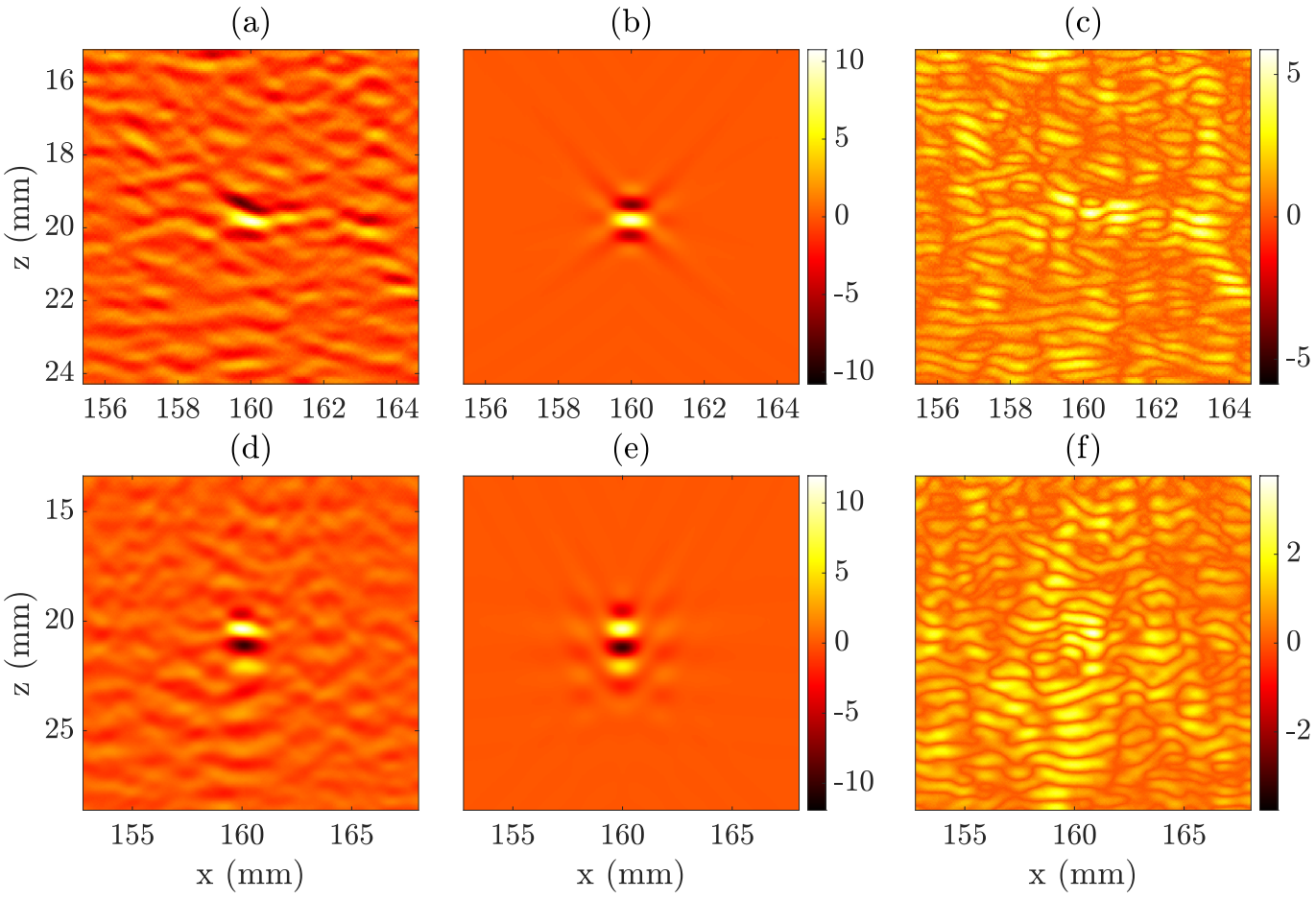

Figure 4: Example of PSF estimation from the SDH located at $z = 20$ mm obtained with 5 MHz data (top row) and with 3 MHz data (bottom row) using the data shown in Figure 3. The first column displays the TFM image centered on the reflector. The second column represents the synthetic PSF reconstructed at the same location by fitting the ultrasonic waveform model. The third column shows the error between the TFM reconstruction and the estimated PSF. Images (a) and (b) have the same dynamic scale. Images (d) and (e) have the same dynamic scale.

the x direction corresponds approximately to the aperture of each probe, that is, 40 mm for the 5 MHz probe and 100 mm for the 3 MHz probe. The imaged zone along the z direction covers the range $[z_{\text{SDH}} - 5\,\text{mm},\ z_{\text{SDH}} + 5\,\text{mm}]$ for the 5 MHz probe, and $[z_{\text{SDH}} - 5\,\text{mm},\ z_{\text{SDH}} + 10\,\text{mm}]$ for the 3 MHz probe, with z_{SDH} the depth of the considered SDH. In all experiments, the pixel size is $0.05 \times 0.05\,\text{mm}^2$. The full images have therefore 801×201 pixels ($40 \times 10\,\text{mm}^2$) for 5 MHz probe, and 2001×301 pixels ($100 \times 15\,\text{mm}^2$) for 3 MHz probe.

4.3. Estimation of the PSF model

Figure 4 (top row) shows the TFM data and the estimated PSF with 5 MHz probe on the single SDH located at $z = 20$ mm. The TFM signature of the SDH looks highly distorted due to the high level of noise. Figure 4 (bottom row) shows the estimated PSF with 3 MHz probe on the same SDH located at $z = 20$ mm. The data have a more regular shape, therefore the main lobes of the ultrasonic waveform are better reconstructed and the estimation error is smaller.

The corresponding time-domain ultrasonic waveform estimated from the 5 MHz data is shown in Figure 5(a), and is almost symmetrical ($r \approx 0$). The estimated waveform with 3 MHz probe is shown in Figure 5(b). In this case, the estimated decay rate is 4.5 times larger on the left part than on the right part, proving the relevance of the asymmetric model.

Finally, for each TFM image, the model (5) with spatially variant PSF along the x direction is considered, based on the PSF obtained in Section 4.3 and taking the acquisition geometry into account (details can be found in [14]).

4.4. Results with the 5 MHz probe

We now present the results obtained with the 5 MHz probe. The computation of the 801×201-pixel TFM beamformed image required 0.12 s, and the inversion procedure required an additional 0.44 s. The estimation of the time-domain waveform parameters and of the 2D PSF are not included in the computation time, since they can be performed in advance within a calibration step. For each pair of SDHs, image

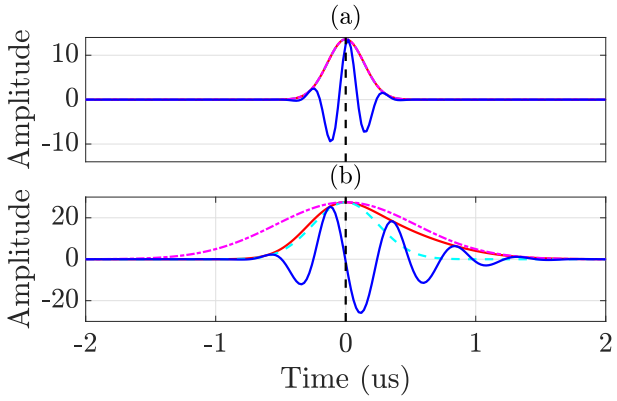

Figure 5: Ultrasonic waveform estimated from the SDH located at 20 mm depth with 3 MHz probe (-), asymmetric Gaussian envelope of the estimated ultrasonic waveform (-), symmetric Gaussian envelope for the left part $\alpha(1+r)$ (– –), symmetric Gaussian envelope for the right part $\alpha(1-r)$ (– -).

5 MHz data			TFM		INV	
z (mm)	SNR (dB)	$\mathcal{R}$ (mm)	γ (dB)	d (mm)	γ (dB)	d (mm)
10	30.37	0.79	−1.94	0.85	$-\infty$	0.95
20	20.90	1.01	0	NR	$-\infty$	0.90
30	14.94	1.30	0	NR	$-\infty$	0.95
40	14.16	1.63	0	NR	0	NR
3 MHz data			**TFM**		**INV**	
z (mm)	SNR (dB)	$\mathcal{R}$ (mm)	γ (dB)	d (mm)	γ (dB)	d (mm)
10	29.02	1.18	0	NR	$-\infty$	0.50
20	23.56	1.25	0	NR	−25.33	0.70
30	20.99	1.35	0	NR	−20.96	0.85
40	16.83	1.48	0	NR	−14.80	0.75

Table 2
Results for the 5 MHz probe (top) and the 3 MHz probe (bottom): data characteristics, PCID γ and estimated distance d between the two reflectors, when detected. The true distance between reflectors is 0.80 mm. NR stands for "Not Resolved".

zooms of 121×121 pixels are displayed, corresponding to 6×6 mm^2. In order to quantify the separation between the flaws, we use the Peak to Center Intensity Difference (PCID) value [22], denoted γ, which is the difference in dB between the maximum amplitude due to the two reflectors and the minimum amplitude in the area between them. This PCID is computed on the line profile obtained by averaging the pixel values over the z axis in each 121×121-pixels image. Two reflectors are considered as resolved if their PCID is lower than -6 dB [22].

Reconstructed images are shown on the top part of Figure 6, together with the line profile corresponding to the average intensity over the corresponding z values. For the SDH pair at 10 mm depth (Figure 6(a)), with SNR $=$ 30.4 dB, the TFM image shows two distinct maxima, with PCID γ slightly below -6 dB, so the two SDHs can be considered as resolved. This observation is consistent with the fact that, in this configuration, the center-to-center distance (0.80 mm) is very close to the Rayleigh criterion ($\mathcal{R} = 0.79$ mm). The INV image shows a clear separation between the two reflectors, and the distance between them is estimated at 0.95 mm, which is close to the true distance (0.80 mm).

Results for the pairs of SDHs at 20 mm and 30 mm depths are presented in Figures 6(b) and 6(c), respectively. Here, the SNR equals 20.9 dB and 14.9 dB, and the Rayleigh criterion equals 1.01 mm and 1.30 mm, respectively, so that the problems are more difficult than at $z = 10$ mm. Similar conclusions can be drawn for both cases: as expected, TFM is not able to resolve the reflectors, whereas the INV method can separate them ($\gamma < -6$ dB). The estimated distance between reflectors is 0.90 mm and 0.95 mm, respectively.

Finally, results for the deepest SDHs ($z = 40$ mm) are displayed in Figure 6(d). In this configuration, one has $\mathcal{R} = 1.63$ mm, which is twice the distance between the reflectors. Due to the high noise level (SNR $=$ 14.2 dB), none of the two methods is able to separate the reflectors.

Numerical results are summarized in Table 2. The pair at 40 mm seems to be the separation limit of the proposed method for this configuration (probe and reflector distance).

4.5. Results with the 3 MHz probe

The bottom part of Figure 6 similarly displays the results obtained with the 3 MHz data. Note that the reconstructed image is much larger in this case ($2\,001 \times 301$ pixels), therefore the computation time for the INV method is now about 20 s (the computation of the TFM image required 0.23 s). For the first SDH pair at $z = 10$ mm, due to the lower frequency of the probe, the Rayleigh criterion is now increased to $\mathcal{R} = 1.18$ mm, and the TFM is not able to resolve the reflectors. On the contrary, the INV method achieves a good separation. Note, however, that the distance between the SDHs is underestimated (0.50 mm). For data at depths 20 mm and 30 mm (see columns (b) and (c) in Figure 6), for which $\mathcal{R} = 1.25$ mm and 1.35 mm respectively, the SDH pairs are well resolved with the INV method, contrary to the TFM. Moreover, the distances between the SDHs in the INV image are quite accurate, 0.70 mm and 0.85 mm respectively. Finally, Figure 6(d) shows that the SDHs can still be resolved by INV since local maxima are found in the image. However, in the last two cases, several artifacts are visible, which may be due to a lower accuracy of the PSF estimation.

Results are summarized in Table 2. We note that, for the three last depths, the distance between the flaws is accurately estimated. Compared to results with 5 MHz data, better performance is achieved with INV, in consistence with the observation that images are less corrupted by structural noise for lower frequencies.

5. Conclusion

We have presented a deconvolution method for resolution improvement in NDT applications. In particular, we have shown that it is well adapted to the inspection of coarse-

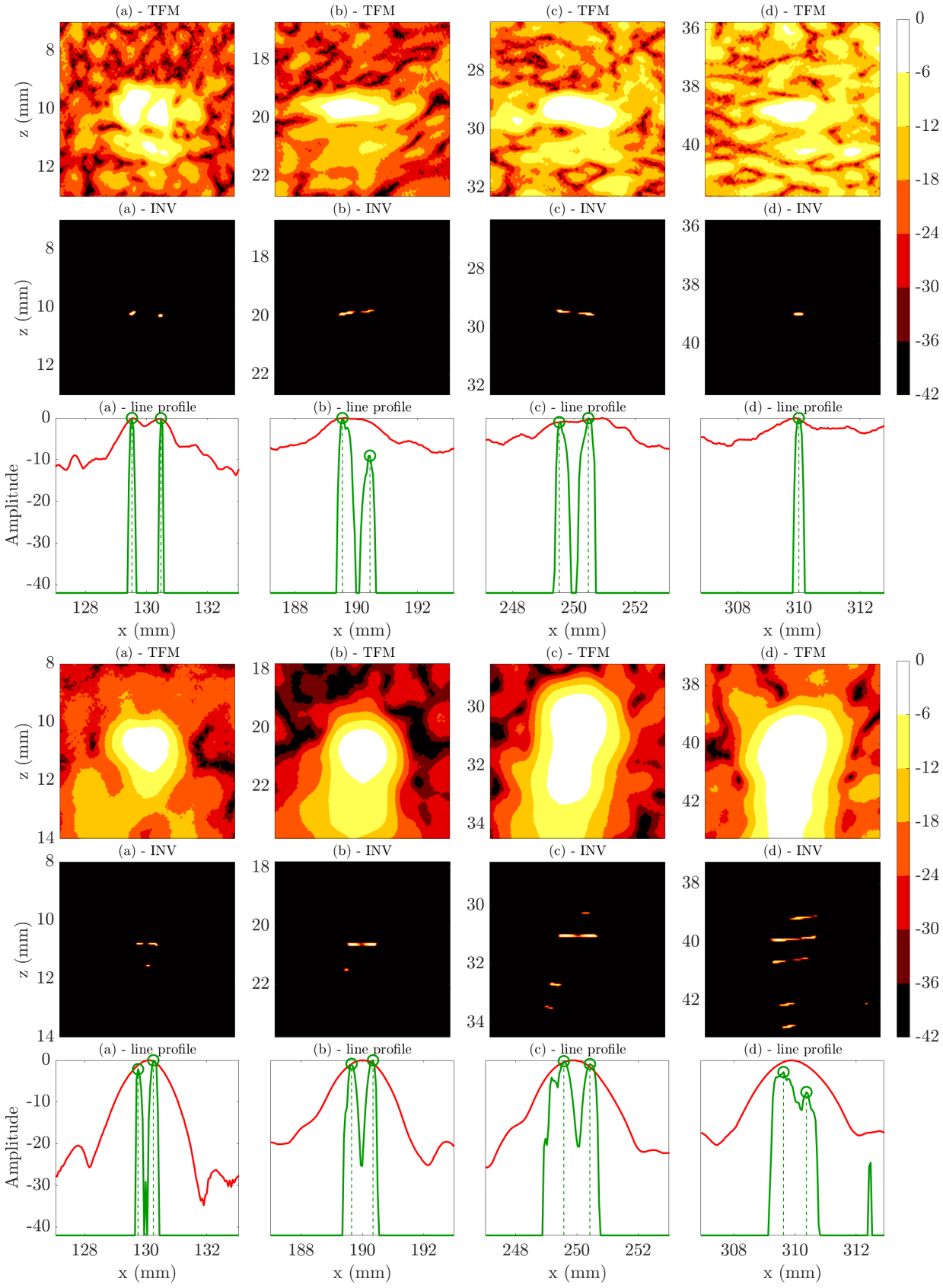

Figure 6: Results obtained with 5 MHz data (5 MHz probe, top panel) and with 3 MHz data (3 MHz probe, bottom panel). In each case, the first row displays the TFM images obtained around each pair of reflectors at depths 10 mm (a), 20 mm (b), 30 mm (c) and 40 mm (d). The second row displays the INV images. The third row represents the image intensity averaged along the z axis, for the TFM image (–) and for the INV image (–).

grained structures, that is a frequent problem in several industry sectors. The method is based on the deconvolution of delay-and-sum beamformed images *e.g.*, TFM, but it could be applied to other acquisition schemes. Experimental results have shown that the resolution capability is increased compared to TFM, going beyond the limit of the Rayleigh criterion. In presence of high-level structural noise, the proposed method is able to separate close reflectors up to about three times the Rayleigh criterion.

This method advantageously enables the use of lower-frequency probes (around 3 MHz) for the inspection of coarse-grained steel samples, for which the ultrasonic pulse propagates farther in the inspected material and therefore provides data with better signal-to-noise ratio. The loss in resolution is then compensated by taking an accurate forward model into account and by enforcing the sparsity of the reconstructed reflectivity image.

The computation time of the proposed method increases with the size of the reconstructed image. In the proposed experiments, a very small pixel size was used ($0.05 \times 0.05\,\mathrm{mm}^2$) in order to achieve high resolution, so that reconstructing the $100 \times 15\,\mathrm{mm}^2$ image with the 3 MHz probe required about 20 s. The computation time could be significantly reduced by reconstructing the images only locally in regions of interest that could be identified from the TFM image. Note that the computational complexity of the method does not depend on the number of transducers, since it works on the precomputed TFM data.

An interesting perspective will concern the applications to more complex reflectors and to real flaws such as porosities and cracks. Indeed, such kind of flaws are supposed to be modeled by more complex point-like responses (*i.e.* PSFs), which have to be experimentally determined. For the results presented in this paper, the elementary waveform has been estimated for each depth. An accurate modeling of the elementary waveform deformation during the propagation in coarse-grained materials [1, 2] would also achieve a reliable forward model, without resorting to an empirical calibration step.

Acknowledgment

This work was partially funded by the French ANRT (Association Nationale Recherche Technologie), project 2017/1083.

References

[1] E. P. Papadakis, Ultrasonic attenuation caused by scattering in polycrystalline metals, The Journal of the Acoustical Society of America 37 (1965) 711–717.

[2] S. Hirsekorn, P. Van andel, U. Netzelmann, Ultrasonic methods to detect and evaluate damage in steel, Nondestructive Testing and Evaluation 15 (1998) 373–393.

[3] M. T. Anderson, S. L. Crawford, S. E. Cumblidge, K. M. Denslow, A. A. Diaz, S. R. Doctor, Assessment of Crack Detection in Heavy-Walled Cast Stainless Steel Piping Welds Using Advanced Low-Frequency Ultrasonic Methods, Technical Report PNNL-16292, NUREG/CR-6933, 921260, 2007. doi:10.2172/921260.

[4] V. Perrot, M. Polichetti, F. Varray, D. Garcia, So you think you can DAS? A viewpoint on delay-and-sum beamforming, Ultrasonics 111 (2021) 106309.

[5] R. Chiao, L. Thomas, Analytic evaluation of sampled aperture ultrasonic imaging techniques for NDE, IEEE Transactions on Ultrasonics, Ferroelectrics and Frequency Control 41 (1994) 484–493.

[6] C. Holmes, B. W. Drinkwater, P. D. Wilcox, Post-processing of the full matrix of ultrasonic transmit-receive array data for non-destructive evaluation, NDT&E International 38 (2005) 701–711.

[7] A. Aubry, A. Derode, Random matrix theory applied to acoustic backscattering and imaging in complex media, Phys. Rev. Lett. 102 (2009) 084301.

[8] S. Shahjahan, A. Aubry, F. Rupin, B. Chassignole, A. Derode, A random matrix approach to detect defects in a strongly scattering polycrystal: How the memory effect can help overcome multiple scattering, Applied Physics Letters 104 (2014) 234105.

[9] E. Lopez Villaverde, S. Robert, C. Prada, Ultrasonic imaging of defects in coarse-grained steels with the decomposition of the time reversal operator, The Journal of the Acoustical Society of America 140 (2016) 541–550.

[10] J. Idier, Bayesian Approach to Inverse Problems, ISTE Ltd and John Wiley & Sons Inc, London, U.K., 2008.

[11] G. A. Guarneri, D. R. Pipa, F. N. Junior, L. V. R. de Arruda, M. V. W. Zibetti, A sparse reconstruction algorithm for ultrasonic images in nondestructive testing, Sensors 15 (2015) 9324.

[12] N. Laroche, S. Bourguignon, E. Carcreff, J. Idier, A. Duclos, An inverse approach for ultrasonic imaging from full matrix capture data: Application to resolution enhancement in NDT, IEEE Transactions on Ultrasonics, Ferroelectrics, and Frequency Control 67 (2020) 1877–1887.

[13] A. Besson, L. Roquette, D. Perdios, M. Simeoni, M. Arditi, P. Hurley, Y. Wiaux, J.-P. Thiran, A physical model of non-stationary blur in ultrasound imaging, IEEE Trans. Comput. Imaging (2019) 1–1.

[14] N. Laroche, S. Bourguignon, J. Idier, E. Carcreff, A. Duclos, Fast non-stationary deconvolution of ultrasonic beamformed images for nondestructive testing, 2021. URL: https://hal.archives-ouvertes.fr/hal-03147256, working paper or preprint.

[15] J. Zhang, B. W. Drinkwater, P. D. Wilcox, A. J. Hunter, Defect detection using ultrasonic arrays: The multi-mode total focusing method, NDT&E International 43 (2010) 123 – 133.

[16] G. Montaldo, M. Tanter, J. Bercoff, N. Benech, M. Fink, Coherent plane-wave compounding for very high frame rate ultrasonography and transient elastography, IEEE Transactions on Ultrasonics, Ferroelectrics, and Frequency Control 56 (2009) 489–506.

[17] M.-H. Bae, M.-K. Jeong, A study of synthetic-aperture imaging with virtual source elements in b-mode ultrasound imaging systems, IEEE Transactions on Ultrasonics, Ferroelectrics, and Frequency Control 47 (2000) 1510–1519.

[18] B. Friedlander, System identification techniques for adaptive signal processing, Circuits, Systems, and Signal Processing 1 (1982) 3–41.

[19] R. Demirli, J. Saniie, Asymmetric Gaussian chirplet model and parameter estimation for generalized echo representation, Journal of the Franklin Institute 351 (2014) 907–921.

[20] A. Beck, M. Teboulle, A fast iterative shrinkage-thresholding algorithm for linear inverse problems, SIAM Journal on Imaging Sciences 2 (2009) 183–202.

[21] F. Simonetti, Localization of pointlike scatterers in solids with subwavelength resolution, Applied Physics Letters 89 (2006) 094105.

[22] C. Fan, M. Caleap, M. Pan, B. W. Drinkwater, A comparison between ultrasonic array beamforming and super resolution imaging algorithms for non-destructive evaluation, Ultrasonics 54 (2014) 1842–1850.